# Accelerating Multi-Echo Water-Fat MRI with a Joint Locally Low-Rank and Spatial Sparsity-Promoting Reconstruction

Felix Lugauer[1], Dominik Nickel[2], Jens Wetzl[1], Berthold Kiefer[2], Joachim Hornegger[1] and Andreas Maier[1]

**Affiliations:**

1 Pattern Recognition Lab, Department of Computer Science, Friedrich-Alexander-Universität Erlangen-Nürnberg, Erlangen, Germany

2 Siemens Healthcare GmbH, Diagnostic Imaging, Erlangen, Germany

**Notes:**

| | |
|---|---|
| Running Head: | Accelerating Multi-echo Water-Fat MRI |
| Correspondence to: | Felix Lugauer<br>Pattern Recognition Lab,<br>(Department of Computer Science),<br>Friedrich-Alexander-Universität Erlangen-Nürnberg,<br>Martensstr. 3, D-91058 Erlangen, Germany.<br>E-mail: felix.lugauer@fau.de<br>Phone: +49 9131 85 27874<br>Fax: +49 9131 303811 |

**Word count:**

| | | | |
|---|---|---|---|
| Abstract: | 199 | Manuscript: | ca. 5000 |
| Figures: | 8 | Tables: | 3 |
| References: | 47 | | |

## CONTENTS

## ABSTRACT

*Object:* To demonstrate the benefits of using locally low-rank (LLR) regularization for the compressed sensing reconstruction of highly-accelerated quantitative water-fat MRI, and to validate fat fraction (FF) and $R_2^*$ relaxation against reference parallel imaging in the abdomen.

*Materials and Methods:* Reconstructions using spatial sparsity regularization (SSR) were compared to reconstructions with LLR and the combination of both (LLR+SSR) for up to 7-fold accelerated 3-D bipolar multi-echo GRE imaging. For 10 volunteers, the agreement with the reference was assessed in FF and $R_2^*$ maps.

*Results:* LLR regularization showed superior noise and artifact suppression compared to reconstructions using SSR. Remaining residual artifacts were further reduced in combination with SSR. Correlation with the reference was excellent for FF with $R^2 = 0.99$ (all methods) and good for $R_2^*$ with $R^2 = [0.93, 0.96, 0.95]$ for SSR, LLR and LLR+SSR. The linear regression gave slope and bias (%) of (0.99, 0.50), (1.01, 0.19) and (1.01, 0.10) and the hepatic FF/$R_2^*$ standard deviation was $3.5\%/12.1\,\mathrm{s}^{-1}$, $1.9\%/6.4\,\mathrm{s}^{-1}$ and $1.8\%/6.3\,\mathrm{s}^{-1}$ for SSR, LLR and LLR+SSR, indicating the least bias and highest SNR for LLR+SSR.

*Conclusion:* A novel reconstruction using both spatial and spectral regularization allows to obtain accurate FF and $R_2^*$ maps for prospectively highly-accelerated acquisitions.

**Key words: Multi-echo Dixon, Quantitative water-fat MRI, Fat fraction, Locally low-rank (LLR), Compressed sensing.**

## INTRODUCTION

In recent years, chemical-shift-encoded water-fat imaging has become a clinical tool for quantitative imaging of the fat-fraction (FF) and relaxation rate ($R_2^*$), enabling the non-invasive assessment of steatosis and iron deposits [1, 2]. These achievements originate from the Dixon method that marked the beginning of water-fat imaging [3]. Unlike MR spectroscopy that is known to accurately quantify fat but is restricted to a small sampling volume, the Dixon method made imaging with a large coverage and high spatial resolution possible [4].

Since then, this method has steadily been improved, both in terms of acquisition efficiency and signal-to-noise ratio (SNR), for instance through multi-point Dixon as well as parallel imaging (PI) with bipolar readouts [5, 6]. Accounting for confounding factors such as $T_1$ bias, a single-peak fat spectrum and relaxation effects allowed for quantitative water-fat magnetic resonance imaging (MRI) [7, 8]. As such, quantitative Dixon required a multi-echo acquisition with longer echo trains [9]. After the advent of compressed sensing (CS) in MRI [10], accelerated multi-echo water-fat imaging was first addressed by Doneva et al. [11]. A novel blipped sampling pattern was combined with a k-space (model-)based water-fat reconstruction, which directly enforces sparsity of water and fat as well as smoothness of the phase map. Consequently, $R_2^*$ estimation was included next and CS was combined with PI (CS-PI), i.e. the acquisition and reconstruction using multiple coils, where Wiens et al. evaluated blipped sampling for the first time prospectively [12, 13]. An alternative k-space based CS reconstruction exploited the correlation across multi-coil measurements for calibrationless (CLEAR) water-fat separation [14].

Generally common to model-based reconstructions is that physical effects such as $R_2^*$ or eddy current effects need to be modeled and considered explicitly during reconstruction. This adds further non-linear complexity, which makes these approaches considerably harder to solve and sensitive to parameter initialization. In fact, a k-space based reconstruction, which also models eddy currents caused by bipolar readouts has not yet been proposed. Alternatively, bipolar imaging was shown to be applicable in combination with a dedicated PI acquisition and reconstruction scheme such that adverse phase effects cancel each other [15]. That being said, the particular advantage of model-based reconstructions is the simultaneous use of data from all echoes and the ability to directly constrain water-fat parameters during reconstruction. This has not been shown to be feasible with conventional two-step, image-based water-fat separation, where echo images are first reconstructed, followed by a separate but quite robust parameter fitting that imposes the water-fat signal model after image reconstruction. As such, this approach allows for $R_2^*$-resolved, quantitative imaging and supports fast bipolar readouts since it offers the flexibility to model physical effects such as field inhomogeneities and eddy currents conveniently during parameter fitting.

Recently, an image-based water-fat separation using CS-PI based on wavelet sparsity in the spatial domain was introduced and demonstrated accurate fat quantification for up to 4- and 5-fold acceleration in liver and muscle imaging [16, 17]. Apart from utilizing faster bipolar readouts, which became common practice for multi-echo GRE imaging, further acceleration can be expected from constraining the signal variation of the echo image series. In order to also benefit from the sparsity along the echo dimension, we extend the CS-PI reconstruction by a model-consistent spectral regularization, which simultaneously regularizes over all available data to promote a low-rank constraint of locally correlated multi-echo images. The idea is to promote consistency in between multi-TE images by enforcing a representation with few chemical components but without knowing the spectral properties of these components. The relationship between echoes has been employed earlier for denoising multi-echo data using local singular value decompositions (SVDs) [18]. Lately, a closely-related automated locally low-rank (LLR) regularization for water-fat imaging and relaxometry obtained denoised parameter maps with a strong SNR gain [19, 20], and proved beneficial on clinical data [21]. The LLR regularization was originally proposed for dynamic MRI reconstruction of the heart but had also been applied to accelerate parameter mapping [22, 23]. Recently, an echo-coupled reconstruction based on LLR regularization showed promising results towards higher acceleration of multi-echo water-fat imaging [24]. The paper at hand extends this earlier work.

After having justified the LLR property for multi-echo water-fat imaging, we describe a joint LLR and spatial sparsity-enforcing (SSR) regularization for CS-PI reconstruction. Our constrained optimization framework targets 3-D multi-echo data from bipolar readouts and does not require modeling of physical effects for the reconstruction, thereby supporting arbitrary subsequent water-fat separation including those based on $R_2^*$ and eddy-current correction. For up to 7-fold prospectively accelerated in-vivo acquisitions, the joint spectral and spatial sparsity regularization LLR+SSR is compared against separate LLR and spatial sparsity regularization. The agreement between reconstructions from undersampled data and a clinically applied Dixon protocol with high resolution is validated by experiments in 10 volunteers, which includes a quantitative analysis of fat fraction and $R_2^*$ maps.

## MATERIALS AND METHODS

We propose to obtain water, fat and $R_2^*$ values in two independent steps. First, the sparsely sampled multi-echo series is reconstructed with a novel regularization framework which makes use of the limited number of independent spectral components across echo images. Second, the reconstructed data is fitted voxel-wise to a common non-linear water-fat model.

### Low-Rank Property of Water-Fat Imaging

The acquisition of multiple images at varying echo times allows the separation of water and fat components based on their difference in resonance frequency due to the differing shielding in fat-bound hydrogen. The relation between individual echo images $\boldsymbol{x}_e, e \in [1, E]$ at echo time $t_e$ with E the number of echo times, and the spectral components water and fat $\boldsymbol{w}$, $\boldsymbol{f} \in \mathbb{C}^N$ can be modeled as

$$\boldsymbol{x}_{e,j} = \left(\boldsymbol{w}_j + \boldsymbol{c}_e \boldsymbol{f}_j\right) \mathrm{e}^{\mathrm{i}\boldsymbol{\Phi}_{e,j}},\ j = 1 \ldots N,\ e = 1 \ldots E, \tag{1}$$

for the $j$-th out of $N = N_x \cdot N_y \cdot N_z$ voxels. The modulation term for the fat component, $\boldsymbol{c}_e = \sum_m \alpha_m \mathrm{e}^{i 2\pi \Delta f_m t_e}$, can be derived from a pre-calibrated multi-peak fat spectrum, where $\alpha_m$ is the known relative amplitude and $f_m$ the frequency shift of the $m^{\text{th}}$ fat peak [25]. Various phase effects originating from field inhomogeneities, gradient delays and eddy currents are modeled by $\boldsymbol{\Phi} \in \mathbb{C}^{N \cdot E}$. The relaxation rate $R_2^*$ is included in the imaginary part of the phase component and allows to identify rapid signal decline due to iron deposits. In order to capture the relaxation in a clinical range, the acquisition of multiple echoes is required [7].

Following this general definition, the signal evolution for multiple echoes is determined by the two spectral components water and fat as well as the phase variation $\mathbf{\Phi}$. A common assumption is that the phase variation is locally smooth [11, 26, 27]. For very small local regions, it can consequently be considered constant. Thus, for an echo train of length greater than two, a spatiospectral matrix that is formed by vectors from locally related samples of each echo will be rank deficient, as the signal is primarily a linear combination from two spectral contributions. Figure 1 demonstrates this pattern for an exemplary multi-echo GRE sequence subject to sufficiently small patches. For water-fat imaging, this LLR property means that the first two singular values and their respective singular vectors contain significant information about the dominating components while the remaining data consists of phase variation and noise. One way to exploit this phenomenon for reconstruction is to regularize these spatiospectral matrices via nuclear norm minimization, which was chosen as it provides the closest convex functional to rank minimization [28]. Defined as the sum of singular values, the nuclear norm is based on a complex-valued singular value decomposition (SVD) of the signal and, thus, preserves phase information as opposed to a magnitude-based SVD. Figure 2 visualizes the singular value distribution of small and larger patches at tissue interfaces with strong phase variations. The rank seems to be unaffected by susceptibilities for the chosen patch sizes, which seems reasonable as the complex-valued representation of spectral components can each carry different phase information, thereby not adding to the rank. This is shown for patches containing the liver, both fat and muscle as well an additional air interface.

## CS-PI Multi-Echo Reconstruction

The straightforward application of CS to multi-echo acquisitions for water-fat imaging is the independent reconstruction of each individual echo followed by a conventional water-fat separation via a non-linear parameter fitting. While this two-step approach is established and quite flexible, the redundancies within the echo series are left unexploited. We propose to take advantage of the LLR property of the signal series by coupling the reconstruction of all echoes in a CS optimization based on nuclear norm minimization of the locally correlated signal [22]. Let $\boldsymbol{x} = [\boldsymbol{x}_1^T, \ldots, \boldsymbol{x}_E^T]^T \in \mathbb{C}^{N \cdot E}$ be the concatenated vector comprising the target image sequence we wish to recover based on $E$ multi-echo and $C$ multi-coil

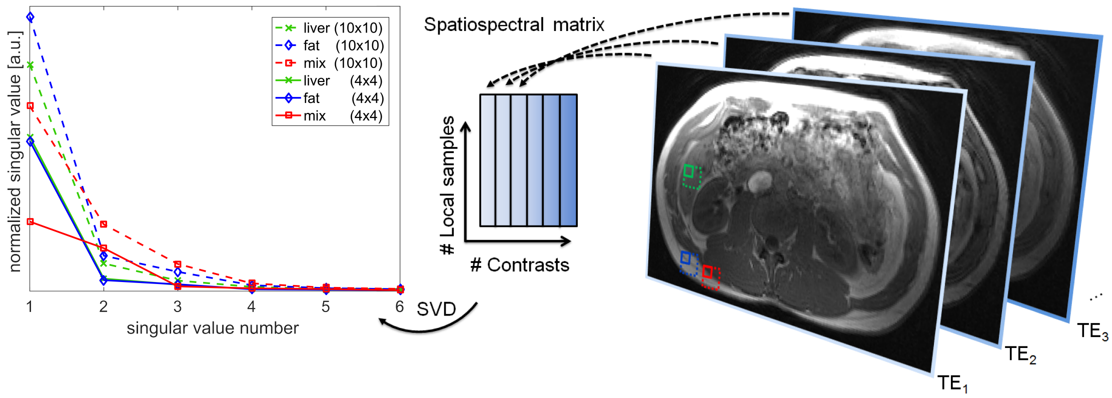


**FIG. 1** Spatiospectral matrices of local patches from all echoes of a multi-echo series exhibit a low-rank singular value distribution. For small patch sizes, the rank is limited by the number of independent spectral components within a patch (water, fat or mixture of both). This effect is more prominent for smaller patches, compare size $4 \times 4$ (solid lines) against $10 \times 10$ (dashed lines). Singular values are normalized by patch size

measurements with each $K$ sampled k-space points $\boldsymbol{y}_{c,e} \in \mathbb{C}^K$:

$$\hat{\boldsymbol{x}} = \underset{\boldsymbol{x}}{\operatorname{argmin}} \sum_{e=1}^{E} \sum_{c=1}^{C} \frac{1}{2} \|\boldsymbol{A}_c \boldsymbol{x}_e - \boldsymbol{y}_{c,e}\|_2^2 + \overbrace{\lambda_b \sum_{p \in \Omega} \|B_p(\boldsymbol{x})\|_*}^{\text{LLR}} + \overbrace{\Psi(\boldsymbol{x}, \lambda_d, \lambda_w)}^{\text{SSR}}, \tag{2}$$

where $\boldsymbol{A}_c$ is the system matrix for coil $c$, which multiplies the image vector with the respective coil sensitivity map and applies the undersampled Fourier transform in order to match the acquired k-space data. The block operation $B_p : \mathbb{C}^{N \cdot E} \to \mathbb{C}^{P \times E}$ extracts $P = P_x \cdot P_y \cdot P_z$ samples ($E \ll P \ll N$) from a local neighborhood $p \in \Omega$ of each echo image and reformats them as column vectors of a spatiospectral matrix. Then, the LLR regularization is given as the summation of the nuclear norm—defined as the sum of singular values—over the set of all neighborhoods $\Omega$. $\Psi$ describes a joint spatial sparsity constraint based on total variation (TV) and a discrete wavelet transform (DWT):

$$\Psi(\boldsymbol{x}, \lambda_d, \lambda_w) = \lambda_d \|(\nabla_x \boldsymbol{x}, \nabla_y \boldsymbol{x})\|_2 + \lambda_w \|\boldsymbol{W}\boldsymbol{x}\|_1, \tag{3}$$

where $\|(\nabla_x \boldsymbol{x}, \nabla_y \boldsymbol{x})\|_2 = \sum_j \sqrt{(\nabla_x \boldsymbol{x})_j^2 + (\nabla_y \boldsymbol{x})_j^2}$ denotes the 2-D isotropic TV formulation and $\boldsymbol{W}$ a redundant DWT [29, 30]. The Lagrange multipliers $\lambda_{\{b,d,w\}}$ balance the influence of each regularization term in relation to the data fidelity term. The motivation for minimizing additional $\ell_1$-terms of sparse or compressible signal representations such as

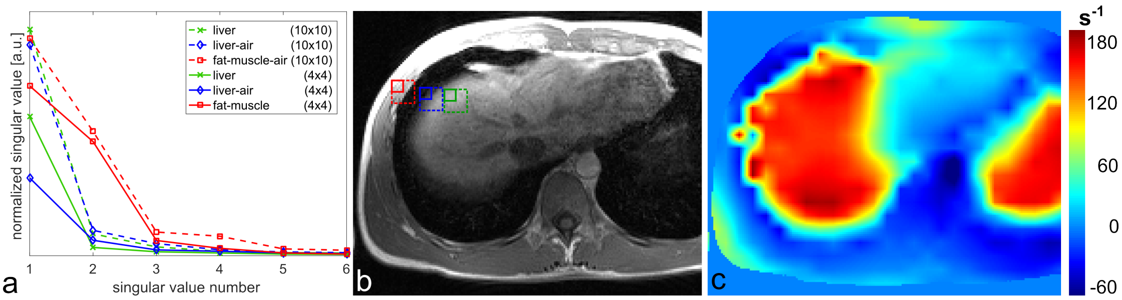


**FIG. 2** The singular value distribution (a) is visualized for various tissue boundaries (b) and for smaller (solid) and larger (dashed) patch sizes, along with the fieldmap (c). The LLR property of a spatiospectral matrix seems to be unaffected by strong fieldmap variations, e.g. due to susceptibility changes at tissue-air interfaces since it is based on the complex-valued SVD, which preserves the phase information

finite differences is fundamental for CS, as it alleviates the problem of finding a unique solution in the underdetermined case of limited measurements data [10]. Joint sparsity by combining TV and wavelet regularization has previously demonstrated to yield improved image quality [29, 31]. The method is denoted SSR when only spatial sparsity is enforced ($\lambda_d$, $\lambda_w > 0 \wedge \lambda_b = 0$). By also promoting the signal to be generated from a limited number of spectral components via the LLR regularization across the echo dimension, further noise reduction and, thus, higher SNR is targeted. In what follows, this is referred to as the LLR+SSR method ($\lambda_d$, $\lambda_w, \lambda_b > 0$), while LLR denotes the corresponding method for ($\lambda_d$ $= \lambda_w = 0 \wedge \lambda_b > 0$).

## Split Bregman Algorithm

To solve the unconstrained optimization problem of the joint LLR+SSR formulation and its variants in Eq. (2), an optimization scheme which is both efficient and versatile by featuring multiple regularization terms is required. *Alternating direction method of multipliers* (ADMM) [32] or Split Bregman (SB) [29] techniques are particularly fast when the problem formulation is separable. The key idea is to split a cost function into parts that consist of either $\ell_2$-terms or proximal operators and alternate between solving the corresponding sub-problems, of which the latter ones can often be solved using component-wise soft-thresholding. Applying the SB scheme for solving Eq. (2) yields an adapted unconstrained cost function with additional proxy variables $\boldsymbol{d}_b \leftarrow \boldsymbol{x}$, $\boldsymbol{d}_x \leftarrow \nabla_x \boldsymbol{x}$, $\boldsymbol{d}_y \leftarrow \nabla_y \boldsymbol{x}$, $\boldsymbol{d}_w \leftarrow \boldsymbol{W}\boldsymbol{x}$ and penalty constraints with their respective Lagrange multipliers $\mu_{\{b,d,w\}}$ for each of the regularizers:

$$\begin{aligned} \hat{\boldsymbol{x}}, \hat{\boldsymbol{d}}_b, \hat{\boldsymbol{d}}_x, \hat{\boldsymbol{d}}_y, \hat{\boldsymbol{d}}_w = \underset{\boldsymbol{x},\boldsymbol{d}_b,\boldsymbol{d}_x,\boldsymbol{d}_y,\boldsymbol{d}_w}{\operatorname{argmin}} & H(\boldsymbol{x}) + \lambda_b \sum_{p\in\Omega} \|B_p(\boldsymbol{d}_b)\|_* + \frac{\mu_b}{2}\|\boldsymbol{d}_b - \boldsymbol{x}\|_2^2 \\ & + \lambda_d \|(\boldsymbol{d}_x, \boldsymbol{d}_y)\|_2 + \frac{\mu_d}{2}\left(\|\boldsymbol{d}_x - \nabla_x \boldsymbol{x}\|_2^2 + \|\boldsymbol{d}_y - \nabla_y \boldsymbol{x}\|_2^2\right) \\ & + \lambda_w \|\boldsymbol{d}_w\|_1 + \frac{\mu_w}{2}\|\boldsymbol{d}_w - \boldsymbol{W}\boldsymbol{x}\|_2^2, \end{aligned} \tag{4}$$

with the data-fidelity term $H(\boldsymbol{x}) = \sum_{e=1}^{E} \sum_{c=1}^{C} \frac{1}{2}\|\boldsymbol{A}_c \boldsymbol{x}_e - \boldsymbol{y}_{c,e}\|_2^2$. Further applying the so called Bregman iteration and generalized split algorithm gives an iterative algorithm that alternates between solving a quadratic problem including data-fidelity and penalty terms as well as proximal operators of their respective $\ell_1$-regularization terms [29]:

$$\begin{aligned} \boldsymbol{x}^{(k+1)} = \underset{\boldsymbol{x}}{\operatorname{argmin}}\, & H(\boldsymbol{x}) + \frac{\mu_b}{2}\|\boldsymbol{d}_b^{(k)} - \boldsymbol{x} - \boldsymbol{b}_b^{(k)}\|_2^2 + \frac{\mu_w}{2}\|\boldsymbol{d}_w^{(k)} - \boldsymbol{W}\boldsymbol{x} - \boldsymbol{b}_w^{(k)}\|_2^2 \\ & + \frac{\mu_d}{2}\left(\|\boldsymbol{d}_x^{(k)} - \nabla_x \boldsymbol{x} - \boldsymbol{b}_x^{(k)}\|_2^2 + \|\boldsymbol{d}_y^{(k)} - \nabla_y \boldsymbol{x} - \boldsymbol{b}_y^{(k)}\|_2^2\right), \end{aligned} \tag{5}$$

$$\boldsymbol{d}_b^{(k+1)} = \underset{\boldsymbol{d}_b}{\operatorname{argmin}} \frac{\mu_b}{2}\|\boldsymbol{d}_b - \boldsymbol{x}^{(k+1)} - \boldsymbol{b}_b^{(k)}\|_2^2 + \lambda_b \sum_{p\in\Omega}\|B_p(\boldsymbol{d}_b)\|_*, \tag{6}$$

$$\boldsymbol{d}_w^{(k+1)} = \underset{\boldsymbol{d}_w}{\operatorname{argmin}} \frac{\mu_w}{2}\|\boldsymbol{d}_w - \boldsymbol{W}\boldsymbol{x}^{(k+1)} - \boldsymbol{b}_w^{(k)}\|_2^2 + \lambda_w \|\boldsymbol{d}_w\|_1, \tag{7}$$

$$\begin{aligned} \left(\boldsymbol{d}_x^{(k+1)}, \boldsymbol{d}_y^{(k+1)}\right) = \underset{\boldsymbol{d}_x,\boldsymbol{d}_y}{\operatorname{argmin}} & \frac{\mu_d}{2}\|\boldsymbol{d}_x - \nabla_x \boldsymbol{x}^{(k+1)} - \boldsymbol{b}_x^{(k)}\|_2^2 \\ & + \frac{\mu_d}{2}\|\boldsymbol{d}_y - \nabla_y \boldsymbol{x}^{(k+1)} - \boldsymbol{b}_y^{(k)}\|_2^2 + \lambda_d \|(\boldsymbol{d}_x, \boldsymbol{d}_y)\|_2. \end{aligned} \tag{8}$$

The procedure for reconstruction is summarized in algorithm 1 and solves the sequence of equations (5)–(8) for $N_{sb}$ iterations or until convergence. While equations (6)–(8) are proximal functions and have known closed form solutions [29, 33], which are given in the Appendix for completeness, Eq. (5) can be solved via gradient-based optimization with conjugate gradient or quasi-Newton algorithms using $N_{l_2}$ gradient steps. Equation (11) performs simple updates on the residual variables $\boldsymbol{b}$ after each iteration to enforce the penalty terms (cf. Appendix).

**Algorithm 1** Split Algorithm for CS Multi-Echo Reconstruction

**Require:** $\boldsymbol{y}, \lambda_{\{b,d,w\}}, \mu_{\{b,d,w\}}, N_{sb}, N_{l_2}$

```
k ← 0
x^(0) ← b^(0)_{b,x,y,w} ← 0
while k < N_sb and ||x^(k) − x^(k−1)||_2 > ε do
    x^(k+1) ← N_l2 iterations of L-BFGS for Eq. (5)
    d^(k+1)_{b,x,y,w} ← { Eq. (12), Eq. (13), Eq. (15), Eq. (16) }    ▷ Shrinkage
    b^(k+1)_{b,x,y,w} ← { Eq. (11) }                                     ▷ Updates
    k ← k + 1
return x^(k)
```

### Poisson Disc Sampling

Incoherent undersampling was obtained using a variable-density Poisson disc sampling. Our variable-density sampling scheme is based on the concept of Bridson to rapidly generate uniform-density Poisson samples [34]. The basic principle is to draw samples starting from an existing sample point and randomly generate up to $R$ points within an annulus of radii $r$ and $2r$ around that position while rejecting points that lie within distance $r$ of existing points. For an extension to variable density, we incorporated a Gaussian density to scale the fixed radius based on the grid position $\boldsymbol{k}$:

$$f_{\mathrm{VD}}(\boldsymbol{k}, \upsilon) = \exp\left(-\frac{(k_y a)^2 + k_z^2}{0.25 N_y^2 \upsilon^{-2}}\right), \tag{9}$$

where the density for a centralized sampling point coordinate $\boldsymbol{k}$ can be adjusted by $\upsilon$. The aspect ratio $a = N_y/N_z$ enables a non-uniform variable density in the phase-encoding plane. The radius before scaling was fixed to $r = 0.634$ such that a dense sampling is obtained at the center and $R = 30$ was used [35]. $\upsilon$ was chosen based on the targeted acceleration factor.

### Acquisition Setup and Volunteer Experiments

All experiments were conducted on 1.5 T and 3 T MR systems (MAGNETOM Aera/Skyra, Siemens Healthcare, Erlangen, Germany) using a prototypical bipolar 3-D GRE (VIBE) sequence. A 6-echo bipolar protocol with 4° flip angle, TR = 9.25 ms and TEs = 1.26,

Table 1. Methods for evaluation with their corresponding parameter setups

| Method | Protocol | AF | TA | $(\lambda_b,\ \lambda_d,\ \lambda_w)$ | $P_x, P_y, P_z$ |
|---|---|---|---|---|---|
| REF | PI CAIPIRINHA | 4 | 19 s | - | - |
| SSR | CS Poisson | 4/6/7 | 19/14/11 s | (0, 0.3, 0.0008) | - |
| LLR | CS Poisson | 4/6/7 | 19/14/11 s | (7, 0, 0) | 4, 4, 1 |
| LLR+SSR | CS Poisson | 4/6/7 | 19/14/11 s | (7, 0.3, 0.0008) | 4, 4, 1 |

2.60, 3.94, 5.28, 6.62, 7.96 ms as well as 1030 Hz/pixel bandwidth was used for both field strengths. The acquired matrix size was $256 \times 188 \times 40$ and was interpolated to $256 \times 208 \times 64$ yielding a voxel size of $1.48 \times 1.48 \times 3.44\,\mathrm{mm}^3$ for a fixed FOV of $38 \times 31 \times 22\,\mathrm{cm}^3$. In addition to the table-mounted spine array, imaging was performed with a flexible 18-channel body array resulting in 26–30 coil elements overall. Separate reference scans for an auto-calibration region of size $24 \times 24$ in the phase-encoding plane were used for calibrating the coil sensitivities and were included in the reported acquisition time (TA).

Abdominal scans were acquired with written consent from 10 volunteers (3 female) whose average age was $39 \pm 15$ years. 6 of these volunteers were scanned with a 1.5 T scanner. The aim of the experiments was to compare conventional imaging and highly accelerated acquisition with incoherent sampling with respect to both image quality and quantification accuracy. For each subject, two scans were acquired: **1)** a reference measurement using CAIPIRINHA sampling [36] with 4× acceleration factor (AF), two in each phase-encoding direction with reorder shift of one, resulting in 19 s TA **2)** a 6× accelerated acquisition in 14 s using a variable-density Poisson disc sampling ($\upsilon = 2.5$).

For one volunteer, two further Poisson sampled acquisitions ($\upsilon = 2.0, 3.0$) resulting in 19 s (4×) and 11 s (7×) scans, were acquired to assess the robustness against varying undersampling.

## Reconstruction Details

Reference acquisitions were directly reconstructed on the scanner system, whereas CS reconstructions were performed offline using a C++ implementation supported by the

Intel® math kernel library and an L-BFGS optimizer for solving Eq. (5) [37]. The k-space measurements from echoes with negative readout polarity were time reversed. Corrections such as linear or higher order phase correction due to the bipolar acquisition were not necessary, as the complex-valued reconstruction is invariant to phase variations in between the echoes. Initially, the acquired data was scaled to the standard normal distribution of noise, which was derived from oversampled readout lines by taking the first and last one percent of samples in central partitions. Coil sensitivity maps were pre-calculated by Hann filtering of the separate reference scan followed by voxel-wise normalization along the channel dimension. The reconstruction of the volumetric+TE data was split into multiple 2-D+TE reconstructions by performing a Fourier transform along the fully-sampled readout. But as we coupled the LLR regularization along the readout and phase-encoding direction, one SB step had to be completed for all 2-D planes before advancing to the next iteration. SSR regularization was applied complementary in the undersampled phase-encoding plane, potentially allowing fully-independent reconstructions. Regarding the block size for the LLR regularization, we found that small block sizes gave the best results. Additionally, the image resolution should be taken into account as blocks along anisotropic image planes showed a smaller denoising effect, probably attributed to the large slice thickness (cf. results). We thus propose $P_x, P_y, P_z = 4, 4, 1$.

While the SB algorithm has more parameters than the original formulation, the penalty parameters $\mu_{\{b,d,w\}}$ merely control the rate of convergence and can be fixed once. Common choices for DWT and TV formulations are $\mu/\lambda = 0.5$ [29]. With $\mu_w/\lambda_w = 0.5$, $\mu_d/\lambda_d = 1$ and $\mu_b/\lambda_b = 0.3$, we found values in a similar range to work best. The regularization weights $\lambda_{\{b,d,w\}}$ were selected empirically based on in-vivo data from a typical acquisition protocol and visual inspection of the water, FF and $R_2^*$ maps with respect to suppression of aliasing and noise artifacts as well as edge preservation (cf. Table 1). Observing the decrease in cost function and visual change in image quality, $N_{sb} = 80$ SB iterations with $N_{l_2} = 2$ were sufficient for the proposed LLR+SSR algorithm. With an Intel® Xeon® E5540 CPU, reconstructions took $80 \pm 7$ min per volume in the case of LLR+SSR.

**Water-Fat Separation.** After reconstructing the complex-valued multi-echo images, a multi-step Dixon algorithm [38] was used in combination with a pre-calibrated multi-peak fat spectrum [25] to extract water and images as well as FF and $R_2^*$ maps. The method successively uses both complex- and magnitude-based signal models in order to refine the solution and obtain a robust estimate. Initially, using only the first two available echoes, a phase-resolved complex-valued estimate for water and fat is obtained [39]. Based on this estimate, water, fat and $R_2^*$ are being re-fitted on the magnitude representation of the signal model in Eq. (1). Here, we used a voxel-wise fitting based on a Levenberg-Marquardt routine with boundary conditions. Note that any magnitude- or complex-based water-fat separation routine is applicable since the proposed reconstruction preserves the phase and the Gaussian noise distribution. Furthermore, the chemical-shift induced shift of fat along the readout was neglected as it was smaller than half a voxel due to the usage of a high receiver bandwidth.

**Translation invariance for blockwise processing.** Similarly to the well-known formation of blocky artifacts when using orthogonal wavelet transforms for denoising, the application of the blockwise nuclear norm for LLR can exhibit similar artifacts [30, 40]. However, a formulation involving the minimization of overlapping patches transforms the problem into an overlapping group lasso, a special case of consensus optimization, which is computationally demanding and has no closed-form solution [41]. Established practical techniques for DWT regularization are either to apply the transform to all shifted version of the signal followed by averaging the processed, unshifted signal, or to perform a single random shift per iteration [30]. The latter approach, known as random cycle spinning, has negligible computational overhead but still provides translation invariance to some degree, and was recently adopted for the blockwise nuclear norm [40]. Yet, this technique was not sufficient for entirely eliminating blocky artifacts in FF maps since residual signal discontinuities are amplified in the fraction calculation. Consequently, we performed an overcomplete processing, which has emerged as one of the key ingredients in current denoising techniques [42]:

$$\boldsymbol{d}^{(k+1)} \approx \operatorname{diag}(\boldsymbol{z})^{-1} \sum_{p \in \Omega^*} B_p^\dagger \left( \operatorname{SVT} \left( B_p \left( \boldsymbol{x}^{(k+1)} \right), \frac{\mu_b}{\lambda_B} \right) \right), \tag{10}$$

using this sliding-window approach with fully overlapping groups $\Omega^*$ yields a translation-invariant approximation of Eq. (6). To this end, $\boldsymbol{z} \in \mathbb{N}_+^{N \cdot E}$ holds the total number of contributing patches at every voxel position such that a fusion or aggregation of overlapping regions is performed as the arithmetic mean.

### Quality Assessment Criteria

Apart from visual inspection of the reconstructed multi-echo and parameter images, various quantitative experiments were used to evaluate the described reconstruction techniques SSR, LLR and LLR+SSR. Edge sharpness measurements were performed on FF maps to assess how the different regularizations affect the results of the water-fat separation. In literature, sharpness is usually defined by the slope of an intensity profile across a prominent edge (organ boundary) using the 20% – 80% intensity rule [43]. Given the maximum $I_{\max}$ and minimum $I_{\min}$ intensity of the intensity profile, the sharpness can be defined via the reciprocal distance between the two points, $A = 0.2(I_{\max} - I_{\min}) + I_{\min}$ and $B = 0.8(I_{\max} - I_{\min}) + I_{\min}$. In order to yield a robust estimate, the final edge sharpness (ES) was computed as the median over a multitude of profiles orthogonal to a manually segmented boundary [44].

Further experiments included a linear regression analysis and were based on mean and standard deviation (SD) for several regions of interest (ROIs) in FF and $R_2^*$ maps. The ROIs were drawn in axial planes of the reference and matched with the CS measurement subject to the same anatomical region: 4 ROIs were placed in different liver regions avoiding vessels while 1 ROI included the spleen for reference purposes, as the FF should physiologically be close to zero there. Thus, the average spleen FF was reported to provide a noise comparison. To assess the agreement with a clinical imaging protocol, the ROI mean values of the reference reconstruction (REF) were subtracted from those of the CS methods. This deviation from the reference, averaged over multiple ROIs and subjects, is also referred to as bias. Notice, however, that unlike biopsy, REF provides no gold-standard and is potentially biased itself. Table 1 lists methods and setups of the corresponding reconstructions.

## RESULTS

### Reconstruction Quality Assessment

Figure 4 shows water images as well as FF and $R_2^*$ maps of the abdomen from a conventional measurement with 4× acceleration in comparison to a 6× accelerated CS-based acquisition with reconstructions from SSR, LLR and LLR+SSR along with their respective undersampling masks. Images of REF are affected by a central noise band, which is particularly visible for FF and $R_2^*$ maps. SSR exhibits less grainy but rather structured or aliased noise, most prominent in the relaxation map where some structures become deteriorated. With the LLR-based methods, the $R_2^*$ map is more smooth though with enhanced structures while FF shows less speckled or aliased noise compared to REF and SSR. The water image for LLR shows a fine graininess as well as Gibbs ringing that was reduced by joint regularization with LLR+SSR. We additionally evaluated the edge sharpness at tissue boundaries between fat and spleen, kidney as well as the liver. Figure 3 visualizes the ES definition and an ES profile for a boundary between fat and the liver. The hatched lines visualize the selected boundaries in the FF map. The median ES of REF is plotted against SSR, LLR and LLR+SSR for various regions. Note that REF and the accelerated methods were manually registered to allow for an evaluation. There is a clear trend between the accelerated methods showing the least ES for SSR and the highest for LLR while LLR+SSR yields values in between.

A quantitative evaluation of in-vivo measurements from all 10 volunteers is provided by Table 2 and Figure 5. Figure 5 plots the linear regression between FF values obtained by the reference and SSR, LLR and LLR+SSR. The regression results in a slope and bias (%) of (0.99, 0.50) for SSR, (1.01, 0.19) for LLR and (1.01, 0.10) for LLR+SSR, which shows a reduction in bias from SSR to LLR over LLR+SSR. Generally, with correlation coefficients of $R^2 = 0.99$ for all methods, there is excellent agreement with the reference. Also, the correlation for $R_2^*$ is good with $R^2 = [0.93, 0.96, 0.95]$ for SSR, LLR and LLR+SSR. Table 2 lists bias and SD of the obtained FF and $R_2^*$ maps of all methods. The deviation from the reference for FF and $R_2^*$ maps is low for all CS-based methods being around 5 to 10 % of typical values in the liver. Yet, the average ROI SDs are relatively high, also for the reference, which indicates a low-SNR acquisition. They are lowest for LLR+SSR, being only one half of that of SSR and around two third of the reference method, which

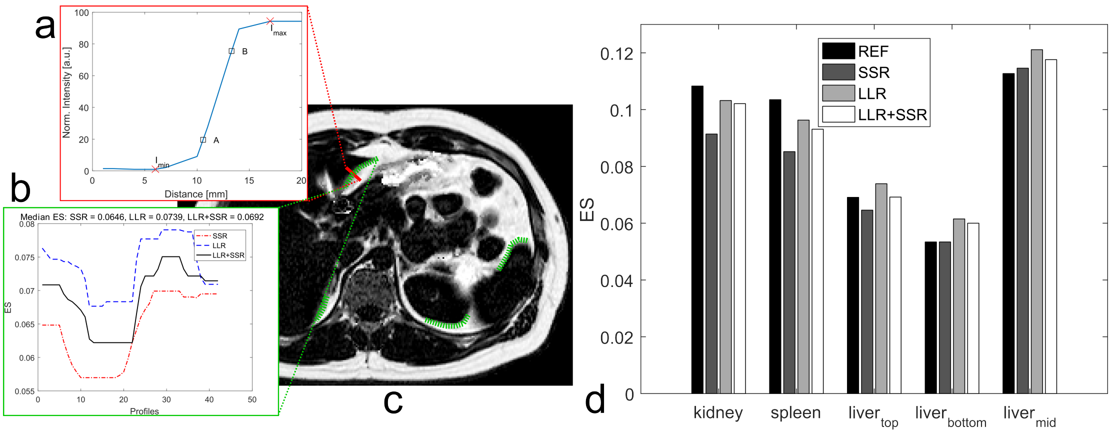


**FIG. 3** Definition of the edges sharpness for an intensity profile across a boundary (a). The sharpness values along a manually segmented boundary ($liver_{top}$ in (d)) are plotted for the accelerated methods (b). Multiple organ boundaries were segmented as marked in the FF map (c) and the corresponding edge sharpness is reported as the median of all profiles along a segment (d)

demonstrates a substantial SNR gain. This noise reduction can also be observed when comparing the FF of the spleen, which is normally close to zero but is around 3 % for the reference and SSR but only 2 % for the LLR-based methods. Using LLR+SSR, the noise-related measures are the lowest and the deviation from the reference is minimal. In conclusion, the proposed method yields quantitatively equivalent results and better SNR for AF 6 in comparison to REF (AF 4).

Figure 6 shows the sampling masks for AFs 4, 6 and 7, as well as images of the $2^{\text{nd}}$ echo and the FF map for the reconstruction methods SSR, LLR and LLR+SSR. In general, noise and the amount of aliasing increase with higher undersampling. Arrows mark the areas in FF and echo images where differences between the methods are most prominent regarding aliasing and detail of structures. The images of SSR exhibit rather speckled, grainy noise for AF 4 while aliasing becomes prominent at higher AFs in FF and echo images. Using LLR, there is no speckled noise in the echo images but slight aliasing and graininess, which increases for higher accelerations. The FF map seems relatively clear at AF 4 while a smoothing effect becomes visible for higher AFs. There is a similar trend for the combined regularization, though graininess and some aliasing or Gibbs-ringing effects

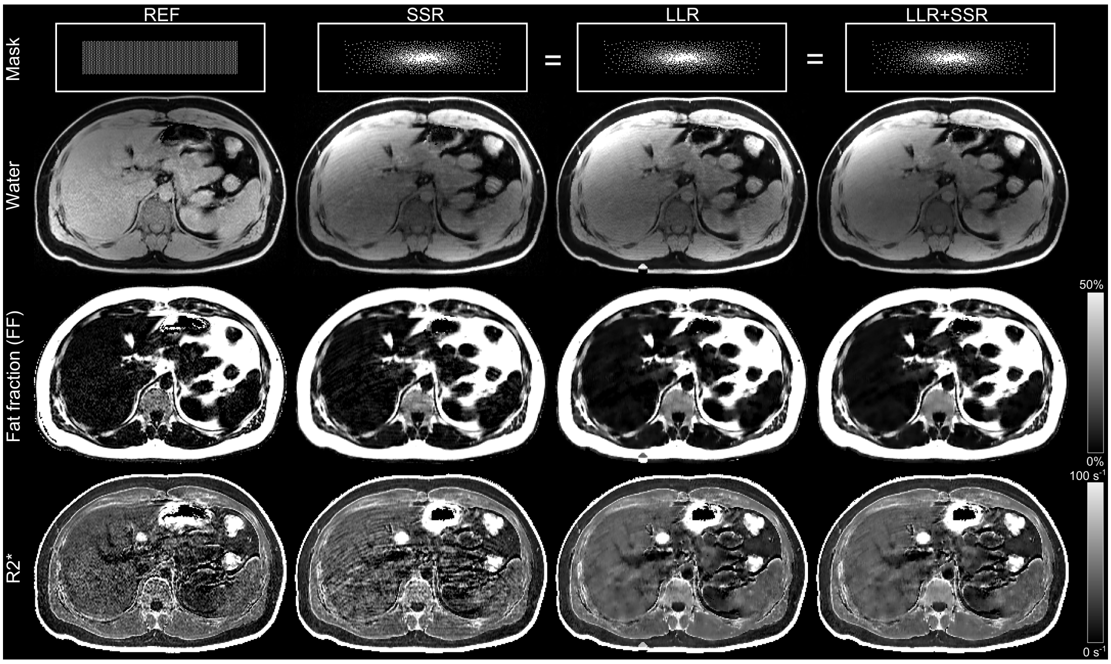


**FIG. 4** Water, FF and $\mathrm{R}_2^*$ images of one volunteer as well as their respective undersampling masks are shown for conventional imaging (19 s) and for a CS acquisition (14 s) using different reconstructions. Both acquisitions are affected by a central noise band and, in the case of CS, additional undersampling aliasing. Note how the different regularizations handle these artifacts and yield quantitative maps of varying quality subject to, e.g., noise amplification and the delineation of structures. Be aware that the images of the CS methods are missing an intensity inhomogeneity correction

are removed in the echo images, which leads to slightly clearer FF maps. In summary, accelerations until AF 4 are feasible with all methods while higher AFs seem restricted to LLR-based methods.

Table 3 summarizes the effect of increasing acceleration factors using a ROI analysis, which was exemplarily performed for one volunteer. The average liver ROI mean and SD were reported for FF and $\mathrm{R}_2^*$ maps as obtained by the previously described methods. The mean FF and $\mathrm{R}_2^*$ values are consistent for all methods at all acceleration factors. The reference acquisition exhibits relatively high SDs for FF and $\mathrm{R}_2^*$ values with $3.6\,\%$ and $11.7\,\mathrm{s}^{-1}$, which are similar to those using SSR at a 4-fold CS acquisition. Comparing the CS-based acquisitions, the FF SD is rising with increasing undersampling from $3.7\,\%$ to

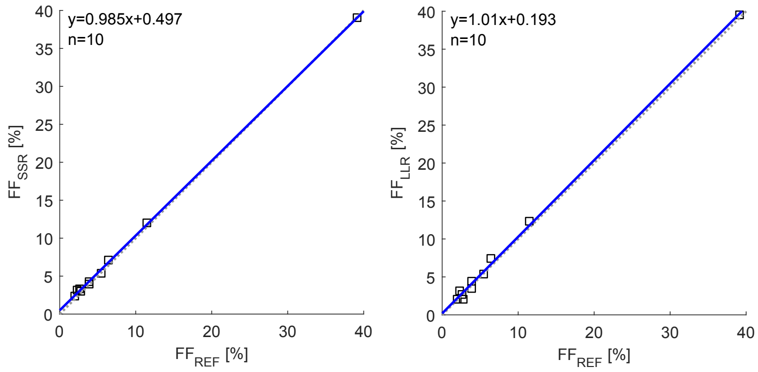


**FIG. 5** Linear regression analysis of the FF between the data reconstructed by REF and the CS methods SSR, LLR and LLR+SSR, in 10 volunteers. Dashed lines represent $y = x$, and solid lines are the linear regression with their formulae at the top left. Data points mark the hepatic FF per volunteer as averaged over 4 ROIs

4.5 % when using SSR but is stable at 1.9 % for the LLR-based methods. The SDs of FF and $R_2^*$ maps are halved compared to the reference at AF 4 and more than halved at AF 6–7 in comparison to SSR.

### Effects of LLR Regularization

A common attempt to find the optimal regularization weight for a regularized optimization is based on the L-curve analysis [45]. Following the L-curve criterion, a plot of the data fidelity term against that of the regularizer for varying regularization weights should have an L-shape. The region with a sharp bend or with the highest curvature is attributed to an effective weight, as here a large reduction of the regularization term is obtained while the fit to the measured data is preserved. Figure 7 plots the cost of the data fidelity term against the cost of the LLR regularizer for an increasing regularization weight $\lambda_b$ after $N_{sb} = 80$ iterations. Next to the curve, we visualized the corresponding reconstruction for a low, the selected and a high $\lambda_b$ according to bend of the curve. The selected weight is a conservative choice for regularization, which is reflected by the similarity to the reconstruction with a low weight. Their difference is only visible in the highly scaled difference image, which shows Gibbs ringing only. In contrast, the closeup of the reconstruction using a high $\lambda_b$ shows loss in contrast and visible blur, which is also supported by the remaining boundaries in their difference image.

Table 2. Deviation from reference and noise evaluation for FF and $R_2^*$ maps of 10 volunteers

| Method | Bias: FF [%] | SD: FF [%] | Bias: $R_2^*$ [$s^{-1}$] | SD: $R_2^*$ [$s^{-1}$] | $FF_{spleen}$ [%] |
|---|---|---|---|---|---|
| REF | - | 2.9 | - | 9.6 | 2.6 |
| SSR | 0.4 | 3.5 | 3.0 | 12.1 | 3.1 |
| LLR | 0.3 | 1.9 | 2.8 | 6.4 | 2.0 |
| **LLR+SSR** | 0.2 | 1.8 | 2.8 | 6.3 | 1.9 |

Deviation from the reference (bias) for FF and $R_2^*$ values from ROIs in the liver was evaluated for SSR, LLR and LLR+SSR relative to a conventional acquisition. For noise assessment, the ROI SDs were averaged over subjects and reported as well as the average spleen FF. Bias and uncertainty measures are high for SSR alone while LLR yields less deviation from REF and distinctly reduced SDs. Closest agreement with REF and lowest noise measures are obtained with LLR+SSR

Figure 8 shows the impact of varying sliding-window parameters of the LLR regularization for FF and $R_2^*$ maps. Utilizing patches that are embedded in the anisotropic sagittal plane is convenient for an efficient readout-decoupled processing but can lead to vertical streaks in axial view. Here, these streaks blur tissue boundaries and result in elevated FF values in comparison to an application in axial plane. Extending the axial regularization over multiple slices also leads to unsuppressed noise and artifacts in $R_2^*$ maps compared to an in-plane processing. Thus, a 2-D axial processing with isotropic patch resolution (e.g., $4 \times 4$ patches) is recommended for 3-D abdominal imaging with a typically large slice thickness.

## DISCUSSION

The advantage of an LLR regularization over conventional spatial regularization has been demonstrated for abdominal CS water-fat MRI. For that, a combined LLR and spatial sparsity regularization (LLR+SSR) was tested against separate regularization with SSR and LLR based on acquisitions from 10 volunteers using up to 7× accelerated Poisson-disc sampling. In contrast to SSR, LLR by itself halved the uncertainty for FF and $R_2^*$ maps and

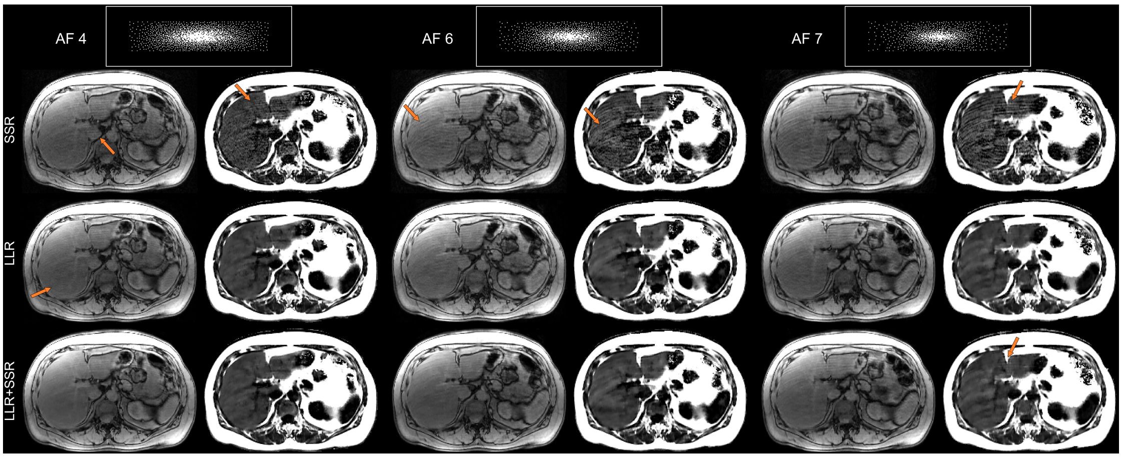


**FIG. 6** For increasing acceleration factors 4, 6 and 7, the sampling mask as well as the 2$^{nd}$ echo and FF map of a volunteer with 13 % liver fat are shown for the reconstruction methods SSR, LLR and LLR+SSR. Generally, noise and the amount of aliasing increases for higher AFs, which can be observed in FF and echo images. Arrows mark areas where differences between the methods are most prominent regarding aliasing and detail of structures

achieved a far better noise performance, i.e. SNR, than the reference acquisition (Tables 2 and 3). This substantial SNR[1] gain can be attributed to the rather low-SNR acquisition setup, which is nevertheless typical for breath-hold limited quantitative measurements [4, 7], and more essentially to the LLR-characteristic denoising: the regularization can be thought of as an averaging along the echo dimension that becomes more effective with the number of echoes [19]. As long as the LLR property is well marked, which is encouraged by using small patches, and later echoes still have enough signal, the LLR regularization has a similar effect to repetitive signal averaging but only with the short extra time for another echo [18]. As such, severe undersampling artifacts, which remained with SSR, were effectively reduced. Yet, LLR alone was not able to completely remove ringing artifacts and subtle graininess. The combination LLR+SSR notably reduced these effects and produced homogeneous tissues while keeping small structures. Although the LLR

[1] As a measure of image noise, SNR is defined as the average signal over the standard deviation in a homogeneous region of interest. Traditionally, higher SNR meant improved image quality. In the light of non-linear algorithms such as CS, it alone cannot serve as universal measure of image quality because reduced noise can simply be induced by reducing image resolution.

Table 3. Effect of increasing acceleration factors evaluated for one subject with elevated fat

| Method | AF 4 | | AF 6 | | AF 7 | |
|---|---|---|---|---|---|---|
| | FF [%] | $R_2^*$ [$s^{-1}$] | FF [%] | $R_2^*$ [$s^{-1}$] | FF [%] | $R_2^*$ [$s^{-1}$] |
| REF | 12.6 ± 3.6 | 38.1 ± 11.7 | - | - | - | - |
| SSR | 12.6 ± 3.7 | 37.1 ± 10.7 | 12.4 ± 4.3 | 40.3 ± 14.5 | 12.7 ± 4.5 | 39.3 ± 14.2 |
| LLR | 12.6 ± 1.9 | 37.4 ± 5.4 | 12.3 ± 1.9 | 39.9 ± 7.5 | 13.0 ± 1.9 | 38.7 ± 6.5 |
| LLR+SSR | 12.7 ± 1.8 | 37.3 ± 5.3 | 12.3 ± 1.9 | 40.1 ± 7.3 | 12.8 ± 1.9 | 38.7 ± 6.4 |

For one volunteer, FF and $R_2^*$ ROIs were compared between the reference and the CS measurement at increasing acceleration factors for different reconstruction methods. Mean ROI values of FF and $R_2^*$ are stable at all acceleration factors for all methods. SDs are halved for the LLR-based methods compared to SSR and REF. While the FF SD for LLR/LLR+SSR is stable at increasing undersampling, it increases with SSR

regularization was selected rather conservative according the L-curve analysis, an effective denoising was achieved while maintaining high agreement with the reference, which is supported quantitatively by the analysis of bias and noise, linear regression as well as edge sharpness.

For LLR, the patch size plays an important role. Generally, a processing with a small local support is supported from a theoretical point of view since the variation in phase is considered smooth and spatially limited [11, 26, 27]. Also, the LLR regularizer has been used previously for denoising and demonstrated the best tradeoff between sharpness and noise reduction for small local patches (5 × 5) [19, 21]. Having observed that the LLR property is particularly well-marked for small 2-D patches in axial slices, and that 3-D processing involving planes with anisotropic resolution can cause sub-optimal denoising, we opt to apply very small patches along isotropic planes only. That being said, the improved noise statistic confirms that the joint application provides complementary denoising, which is superior to separate regularization using either SSR or LLR. Similar performance was demonstrated for acceleration factors from 4 to 7, indicating that the proposed techniques

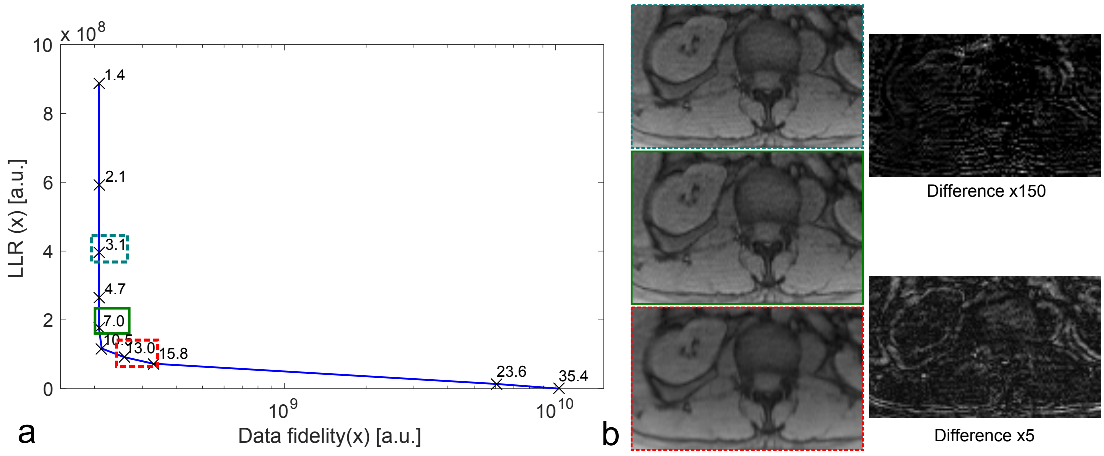


**FIG. 7** L-curve analysis: the LLR regularization term is plotted against the cost of the data fidelity for $\lambda_b = [1.4, 35.4]$. A conservative, the proposed and a high $\lambda_b$ are marked (a). A closeup of the corresponding images of the 5$^{\text{th}}$ echo are shown along with the difference images between the proposed and the conservative, as well as the high regularization weight (b)

are robust enough to possibly support even higher accelerations.

A comparison to previous studies based on statistical values is difficult as the related k-space based water-fat reconstructions provide only data from retrospectively undersampled acquisitions or images were obtained with different resolution and acceleration factors. Commonly reported is the SD of the FF in a region of interest, which can serve to indicate SNR. Considering the k-space methods, Sharma et al. report a FF SD of over 4 % averaged over 7 datasets for AF 4 with a regression equation to the reference of 0.97x+0.25, whereas Wiens et al. lists 1.0/1.4 % on a single dataset for AF 4.2/5 [12, 13]. Regarding image-based water-fat reconstructions and prospective experiments, Mann et al. report a FF bias of -0.1 % and average SD of 0.8 % for AF 4.8, in 11 patients [16]. With a higher intra- and interslice resolution, our method compares excellently with a regression equation of 1.01x + 0.10, an average FF bias of 0.2 % and FF SD of 1.8 % averaged over 10 datasets for AF 6. An advantage over previous work is that the proposed method allows for exploiting the redundancies across the echo dimension as well as reconstructing highly undersampled data without explicitly modeling physical effects such as $R_2^*$ or eddy currents.

Due to the lack of a fully sampled reference acquisition, which is currently unfeasible

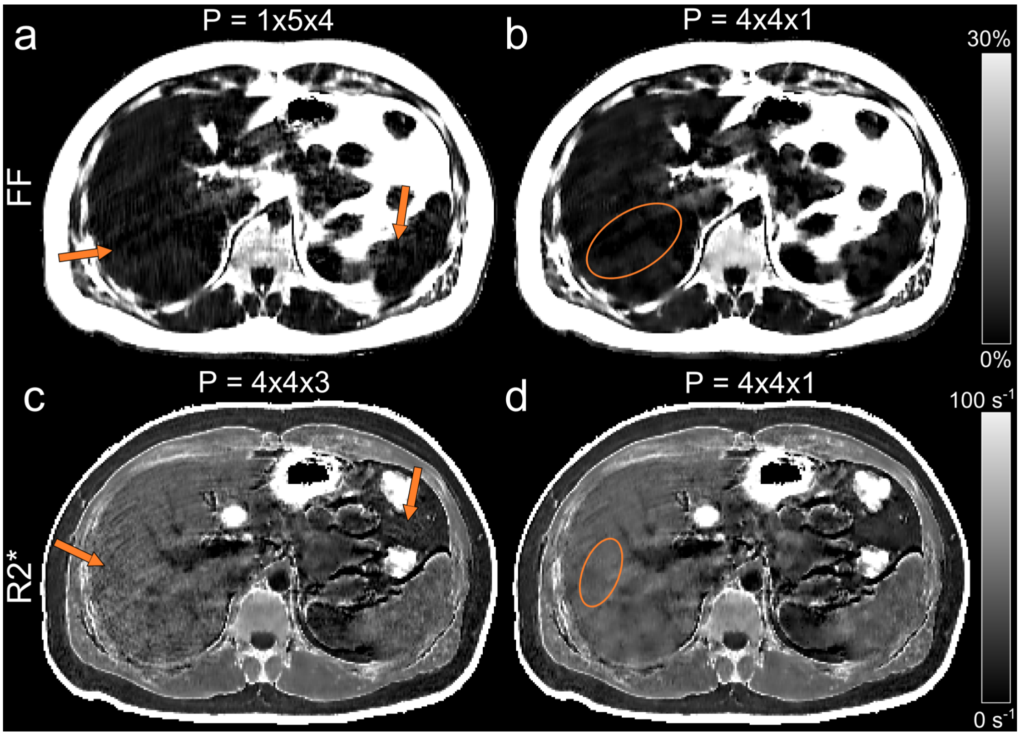


**FIG. 8** LLR regularization with rather quadratic patches in combination with anisotropic resolution can cause non-optimal artifact suppression due to the processing of voxels from a larger physical distance. Here, streaks and isolated spikes occur in the FF map (a). A regularization solely along the isotropic axial plane (b) instead removes this effect and leads to a lower FF with reduced SD ($1.8 \pm 1.5$ % vs. $2.3 \pm 1.7$ %). Similarly, noise reduction and more homogeneous $\mathrm{R}_2^*$ maps can be obtained when LLR processing is restricted to the axial plane (c,d) ($36.6 \pm 4.0$ s$^{-1}$ vs. $36.3 \pm 6.7$ s$^{-1}$)

when both high resolution and short scan times are desired, we utilized an accelerated PI acquisition with high resolution as reference standard. This seems reasonable since fat quantification from PI is considered accurate and is commonly used in abdominal studies, e.g. [38, 46]. Note that we used 1.5 T and 3 T systems only due to practical purposes. No abnormal differences were observed, which is expected as accurate FF quantification can be obtained independent of field-strength [46]. The depicted qualitative results are from a 1.5 T system.

The next step will be the validation of this method on clinical data. While the current study included volunteers with elevated hepatic FF (up to 42 %), there was no validation for pathological $R_2^*$ values. Albeit from a theoretical point of view, a spatially constant (within a given patch) $R_2^*$ does not affect the rank of a spatiospectral matrix, i.e. the LLR regularization, since their columns (echoes) will be scaled as a whole dependent on the rate of relaxation and echo time. Also, a previous study on LLR denoising, which applies a technique similar to LLR regularization but with only one iteration, report that mean FF and $R_2^*$ of 42 clinical datasets were not adversely affected [21]. For future work, an evaluation of other low-rank inducing norms such as non-convex Schatten p-norms$_{(p<1)}$ might be of interest. Even though their convergence is dependent on continuation or initialization schemes, non-convex norms have previously outperformed nuclear norm regularization for certain applications [47]. Furthermore, a large workload percentage of the proposed algorithm including the application of spatial sparsity transforms, proximal operators as well as the data fidelity term would lend itself for parallelism on graphics hardware and could reduce the overall reconstruction time.

## CONCLUSION

The feasibility of highly-accelerated quantitative water-fat MRI using CS-PI with joint spatial and spectral regularization has been demonstrated and validated in 10 volunteers. LLR regularized reconstructions yield accurate quantification with a substantial SNR gain for FF and $R_2^*$ maps in comparison to spatial sparsity regularization and parallel imaging, which can further be improved upon by jointly promoting spectral and spatial sparsity. The improved noise statistic can be spent for accelerating multi-echo data acquisition and consequently for improving the accuracy of SNR-critical parameter fitting.

## APPENDIX: UPDATE TERMS AND SOLUTIONS OF PROXIMAL OPERATORS

Update terms of the SB algorithm enforce the coupling with penalty terms:

$$\begin{aligned}
\boldsymbol{b}_b^{(k+1)} &= \boldsymbol{b}_b^{(k)} + \boldsymbol{x}^{(k+1)} - \boldsymbol{d}_b^{(k+1)}, \\
\boldsymbol{b}_x^{(k+1)} &= \boldsymbol{b}_x^{(k)} + \nabla_x \boldsymbol{x}^{(k+1)} - \boldsymbol{d}_x^{(k+1)}, \\
\boldsymbol{b}_y^{(k+1)} &= \boldsymbol{b}_y^{(k)} + \nabla_y \boldsymbol{x}^{(k+1)} - \boldsymbol{d}_y^{(k+1)}, \\
\boldsymbol{b}_w^{(k+1)} &= \boldsymbol{b}_w^{(k)} + \boldsymbol{W} \boldsymbol{x}^{(k+1)} - \boldsymbol{d}_w^{(k+1)}.
\end{aligned} \tag{11}$$

The proximal operator for the TV formulation is realized via generalized shrinkage as

$$\boldsymbol{d}_x^{(k+1)} = \left(\boldsymbol{s}^{(k)} - \frac{\mu_d}{\lambda_d}\right)_+ \frac{\nabla_x \boldsymbol{x}^{(k+1)} + \boldsymbol{b}_x^{(k)}}{\boldsymbol{s}^{(k)}}, \tag{12}$$

$$\boldsymbol{d}_y^{(k+1)} = \left(\boldsymbol{s}^{(k)} - \frac{\mu_d}{\lambda_d}\right)_+ \frac{\nabla_y \boldsymbol{x}^{(k+1)} + \boldsymbol{b}_y^{(k)}}{\boldsymbol{s}^{(k)}}, \tag{13}$$

with

$$\boldsymbol{s}^{(k)} = \sqrt{\left(\nabla_x \boldsymbol{x}^{(k+1)} + \boldsymbol{b}_x^{(k)}\right)^2 + \left(\nabla_y \boldsymbol{x}^{(k+1)} + \boldsymbol{b}_y^{(k)}\right)^2}, \tag{14}$$

where $(\boldsymbol{a})_+$ performs component-wise $\max(0, \boldsymbol{a}_j)$, while soft-thresholding of wavelet coefficients is used for DWTs [29]:

$$\boldsymbol{d}_w^{(k+1)} = \mathrm{soft}\left(\boldsymbol{W}\boldsymbol{x}^{(k+1)} + \boldsymbol{b}_w^{(k)}, \frac{\mu_w}{\lambda_w}\right). \tag{15}$$

The LLR proximal functional can be solved separately in the case of non-overlapping blocks by singular value soft-thresholding and placing the result back with the adjoint operator $B^\dagger$ [28, 33],

$$\begin{gathered}\boldsymbol{d}_b^{(k+1)} = \sum_{p\in\Omega} B_p^\dagger \left(\mathrm{SVT}\left(B_p\left(\boldsymbol{x}^{(k+1)}\right), \frac{\mu_b}{\lambda_B}\right)\right), \\ \text{using } \mathrm{SVT}(\boldsymbol{X}, \theta) = \boldsymbol{U}\,\mathrm{diag}\left((\boldsymbol{\sigma} - \theta)_+\right)\boldsymbol{V}^T.\end{gathered} \tag{16}$$


## ACKNOWLEDGEMENTS

This work was partly supported by the Research Training Group 1773 "Heterogeneous Image Systems", funded by the German Research Foundation (DFG).


## COMPLIANCE WITH ETHICAL STANDARDS

**Informed consent** This manuscript does not contain clinical studies or patient data. Informed consent was obtained from all volunteers included in the study.

**Conflict of interest** Felix Lugauer and Jens Wetzl receive project funding from Siemens Healthcare GmbH. Dominik Nickel and Berthold Kiefer are employees of Siemens Healthcare GmbH.

## Authors' contribution

- Lugauer: Protocol and project development, data collection and analysis
- Nickel: Protocol and project development, data management
- Wetzl: Data collection and management
- Kiefer: Project development
- Hornegger: Project development
- Maier: Project development

## REFERENCES


[1] Meisamy S, Hines CD, Hamilton G, Sirlin CB, McKenzie CA, Yu H, Brittain JH, Reeder SB (2011) Quantification of hepatic steatosis with T1-independent, T2*-corrected MR imaging with spectral modeling of fat: blinded comparison with MR spectroscopy. Radiology 258(3):767–775

[2] Bashir MR, Zhong X, Nickel MD, Fananapazir G, Kannengiesser SA, Kiefer B, Dale BM (2015) Quantification of hepatic steatosis with a multistep adaptive fitting MRI approach: prospective validation against MR spectroscopy. Am J Roentgenol 204(2):297–306

[3] Dixon WT (1984) Simple proton spectroscopic imaging. Radiology 153(1):189–194

[4] Reeder SB, Cruite I, Hamilton G, Sirlin CB (2011) Quantitative assessment of liver fat with magnetic resonance imaging and spectroscopy. J Magn Reson Imaging 34(4):729–749

[5] Reeder SB, Pineda AR, Wen Z, Shimakawa A, Yu H, Brittain JH, Gold GE, Beaulieu CH, Pelc NJ (2005) Iterative decomposition of water and fat with echo asymmetry and least-squares estimation (IDEAL): application with fast spin-echo imaging. Magn Reson Med 54(3):636–644

[6] Koken P, Eggers H, Börnert P (2007) Fast single breath-hold 3D abdominal imaging with water-fat separation. In: Proceedings of the 15th scientific meeting, International Society for Magnetic Resonance in medicine, Berlin, p 1623

[7] Liu CY, McKenzie CA, Yu H, Brittain JH, Reeder SB (2007) Fat quantification with IDEAL gradient echo imaging: correction of bias from T1 and noise. Magn Reson Med 58(2):354–364

[8] Bydder M, Yokoo T, Hamilton G, Middleton MS, Chavez AD, Schwimmer JB, Lavine JE, Sirlin CB (2008) Relaxation effects in the quantification of fat using gradient echo imaging. Magn Reson Imaging 26(3):347–359

[9] Yu H, Shimakawa A, McKenzie CA, Brodsky E, Brittain JH, Reeder SB (2008) Multiecho water-fat separation and simultaneous R2* estimation with multifrequency fat spectrum modeling. Magn Reson Med 60(5):1122–1134

[10] Lustig M, Donoho D, Pauly JM (2007) Sparse MRI: The application of compressed sensing for rapid MR imaging. Magn Reson Med 58(6):1182–1195

[11] Doneva M, Börnert P, Eggers H, Mertins A, Pauly J, Lustig M (2010) Compressed sensing for chemical shift-based water–fat separation. Magn Reson Med 64(6):1749–1759

[12] Sharma SD, Hu HH, Nayak KS (2013) Accelerated T2*-compensated fat fraction quantification using a joint parallel imaging and compressed sensing framework. J Magn Reson Imaging 38(5):1267–1275

[13] Wiens CN, McCurdy CM, Willig-Onwuachi JD, McKenzie CA (2014) R2*-corrected water–fat imaging using compressed sensing and parallel imaging. Magn Reson Med 71(2):608–616

[14] Sharma SD, Trzasko JD, Manduca A (2013) Calibrationless Chemical Shift Encoded Imaging Using a Time-Segmented k-Space Reconstruction. In: Proceedings of the 21st scientific meeting, International Society for Magnetic Resonance in medicine, Salt Lake City, p 130

[15] Soliman AS, Wiens CN, Wade TP, McKenzie CA (2015) Fat quantification using an interleaved bipolar acquisition. Magn Reson Med 75(5):2000–2008

[16] Mann LW, Higgins DM, Peters CN, Cassidy S, Hodson KK, Coombs A, Taylor R, Hollingsworth KG (2016) Accelerating MR Imaging Liver Steatosis Measurement Using Combined Compressed Sensing and Parallel Imaging: A Quantitative Evaluation. Radiology 278(1):247–256

[17] Hollingsworth KG, Higgins DM, McCallum M, Ward L, Coombs A, Straub V (2014) Investigating the quantitative fidelity of prospectively undersampled chemical shift imaging in muscular dystrophy with compressed sensing and parallel imaging reconstruction. Magn Reson Med 72(6):1610–1619

[18] Bydder M, Du J (2006) Noise reduction in multiple-echo data sets using singular value decomposition. Magn Reson Imaging 24(7):849–856

[19] Lugauer F, Nickel D, Wetzl J, Kannengiesser SA, Maier A, Hornegger J (2015) Robust spectral denoising for water-fat separation in magnetic resonance imaging. In: Medical Image Computing and Computer-Assisted Intervention–MICCAI 2015, Munich, pp 667–674

[20] Lugauer F, Nickel D, Kannengiesser S, Barnes S, Holshouser B, Wetzl J, Hornegger J, Maier A (2016) Improving Parameter Mapping in MRI Relaxometry and Multi-Echo Dixon Using an Automated Spectral Denoising. In: Proceedings of the 24th scientific meeting, International Society for Magnetic Resonance in medicine, Singapore, p 3269

[21] Allen BC, Lugauer F, Nickel D, Bhatti L, Dafalla R, Dale BM, Jaffe T, Bashir M (2016) Effect of a Low-Rank Denoising Algorithm on Quantitative MRI-Based Measures of Liver Fat and Iron. In: Proceedings of the 24th scientific meeting, International Society for Magnetic Resonance in medicine, Singapore, p 4224. Accepted for publication in JCAT

[22] Trzasko J, Manduca A, Borisch E (2011) Local versus global low-rank promotion in dynamic MRI series reconstruction. In: Proceedings of the 19th scientific meeting, International Society for Magnetic Resonance in medicine, Montreal, p 4371

[23] Zhang T, Pauly JM, Levesque IR (2015) Accelerating parameter mapping with a locally low rank constraint. Magn Reson Med 73(2):655–661

[24] Lugauer F, Nickel D, Wetzl J, Kiefer B, Hornegger J (2015) Water-Fat Separation Using a Locally Low-Rank Enforcing Reconstruction. In: Proceedings of the 23rd scientific meeting, International Society for Magnetic Resonance in medicine, Toronto, p 3652

[25] Hamilton G, Yokoo T, Bydder M, Cruite I, Schroeder ME, Sirlin CB, Middleton MS (2011) In vivo characterization of the liver fat 1H MR spectrum. NMR Biomed 24(7):784–790

[26] Berglund J, Ahlström H, Johansson L, Kullberg J (2011) Two-point dixon method with flexible echo times. Magn Reson Med 65(4):994–1004

[27] Cui C, Wu X, Newell JD, Jacob M (2015) Fat water decomposition using globally optimal surface estimation (GOOSE) algorithm. Magn Reson Med 73(3):1289–1299

[28] Cai JF, Candès EJ, Shen Z (2010) A singular value thresholding algorithm for matrix completion. SIAM J Optim 20(4):1956–1982

[29] Goldstein T, Osher S (2009) The split Bregman method for L1-regularized problems. SIAM J Imaging Sci 2(2):323–343

[30] Figueiredo MA, Nowak RD (2003) An EM algorithm for wavelet-based image restoration. IEEE Trans Image Process 12(8):906–916

[31] Hutter J, Grimm R, Forman C, Hornegger J, Schmitt P (2015) Highly undersampled peripheral Time-of-Flight magnetic resonance angiography: optimized data acquisition and iterative image reconstruction. Magn Reson Mater Phy 28(5):437–446

[32] Eckstein J, Bertsekas DP (1992) On the Douglas—Rachford splitting method and the proximal point algorithm for maximal monotone operators. Math Program 55(1-3):293–318

[33] Trzasko JD, Manduca A (2011) Calibrationless parallel MRI using CLEAR. In: 2011 Conference Record of the Forty Fifth Asilomar Conference on Signals, Systems and Computers (ASILOMAR), Pacific Grove, pp 75–79

[34] Bridson R (2007) Fast Poisson Disk Sampling in Arbitrary Dimensions. In: ACM SIGGRAPH 2007 Sketches

[35] Song C, Wang P, Makse HA (2008) A phase diagram for jammed matter. Nature 453(7195):629–632

[36] Breuer FA, Blaimer M, Mueller MF, Seiberlich N, Heidemann RM, Griswold MA, Jakob PM (2006) Controlled aliasing in volumetric parallel imaging (2D CAIPIRINHA). Magn Reson Med 55(3):549–556

[37] Zhu C, Byrd RH, Lu P, Nocedal J (1997) Algorithm 778: L-BFGS-B: Fortran subroutines for large-scale bound-constrained optimization. ACM Trans Math Softw 23(4):550–560

[38] Zhong X, Nickel MD, Kannengiesser SA, Dale BM, Kiefer B, Bashir MR (2014) Liver fat quantification using a multi-step adaptive fitting approach with multi-echo GRE imaging. Magn Reson Med 72(5):1353–1365

[39] Eggers H, Brendel B, Duijndam A, Herigault G (2011) Dual-echo Dixon imaging with flexible choice of echo times. Magn Reson Med 65(1):96–107

[40] Ong F, Lustig M (2016) Beyond low rank + sparse: multiscale low rank matrix decomposition. IEEE J Sel Top Signal Process 10(4):672–687

[41] Boyd S, Parikh N, Chu E, Peleato B, Eckstein J (2011) Distributed optimization and statistical learning via the alternating direction method of multipliers. Found Trends Mach Learn 3(1):1–122

[42] Katkovnik V, Foi A, Egiazarian K, Astola J (2010) From local kernel to nonlocal multiple-model image denoising. Int J Comput Vis 86(1):1–32

[43] Shea SM, Kroeker RM, Deshpande V, Laub G, Zheng J, Finn JP, Li D (2001) Coronary artery imaging: 3D segmented k-space data acquisition with multiple breath-holds and real-time slab following. J Magn Reson Imaging 13(2):301–307

[44] Taubmann O, Wetzl J, Lauritsch G, Maier A, Hornegger J (2015) Sharp as a Tack. In: Bildverarbeitung für die Medizin 2015, pp 425–430. Springer

[45] Hansen PC (1992) Analysis of discrete ill-posed problems by means of the L-curve. SIAM review 34(4):561–580

[46] Artz NS, Haufe WM, Hooker CA, Hamilton G, Wolfson T, Campos GM, Gamst AC, Schwimmer JB, Sirlin CB, Reeder SB (2015) Reproducibility of MR-based liver fat quantification across field strength: Same-day comparison between 1.5 T and 3T in obese subjects. J Magn Reson Imaging 42(3):811–817

[47] Lingala SG, Hu Y, DiBella E, Jacob M (2011) Accelerated dynamic MRI exploiting sparsity and low-rank structure: kt SLR. IEEE Trans Med Imaging 30(5):1042–1054